Evaluation of SSM/I and AMSR-E Sea Ice Concentrations in the Antarctic Spring Using KOMPSAT-1 EOC Images

Hoonyol Lee, *Associate Member, IEEE*, and Hyangsun Han, *Student Member, IEEE*

***Abstract*—To evaluate sea ice concentrations (SICs) from the Special Sensor Microwave/Imager (SSM/I) and Advanced Microwave Scanning Radiometer-EOS (AMSR-E), we observed sea ice with the 6-m-resolution panchromatic electronic optical camera (EOC) sensor onboard the Korea Multi-Purpose Satellite-1 (KOMPSAT-1). A total of 68 cloud-free EOC images were obtained across the Antarctic continental edges from September to November 2005. Sea ice types in the EOC images were classified into white ice (W), gray ice (G), and dark-gray ice (D) and then compared with SSM/I and AMSR-E SICs. Spatiotemporal standard deviation of passive microwave SIC proved useful in selecting temporally stable and spatially homogeneous SICs to overcome the diurnal variation of sea ice in the analysis of data from multiple satellites. In the Antarctic spring, the EOC SIC of W + G showed the best fit to SSM/I SIC calculated by the NASA Team (NT) algorithm (mean difference of −2.3% and rmse of 3.2%), whereas that of W + G + D showed the best fit to AMSR-E SIC calculated by the NT2 algorithm (mean difference of 0.3% and rmse of 1.4%). It is concluded that the SSM/I NT algorithm responds to young ice in addition to the ice types A and B, whereas the AMSR-E NT2 algorithm detects ice type C and thin ice as well. The 4.7% difference of SICs between AMSR-E and SSM/I was attributed to the enhanced detection of ice type C (2.1%) and thin ice (2.6%) of the AMSR-E NT2 algorithm.**

***Index Terms*—Advanced Microwave Scanning Radiometer-EOS (AMSR-E), electronic optical camera (EOC), ice type C, image analysis, Korea Multi-Purpose Satellite-1 (KOMPSAT-1), new ice, passive microwave, sea ice, sea ice concentration (SIC), spatiotemporal standard deviation, Special Sensor Microwave/Imager (SSM/I), thin ice, young ice.**

I. Introduction

THE POLAR regions are an important part of the global climate system. The rapid decrease of sea ice extent and the rise of sea level have been reported as prime indicators of climate change possibly from global warming [1]–[6]. Since the early 1970s, passive microwave sensors have been widely used for satellite remote sensing of the polar region because they are less affected by atmospheric condition or solar radiation than optical sensors.

Manuscript received June 25, 2007; revised November 18, 2007. This work was supported by the Korea Polar Research Institute under Grant PE08020.

The authors are with the Department of Geophysics, Kangwon National University, Chuncheon, Kangwon-do 200-701, Korea (e-mail: hoonyol@kangwon.ac.kr).

Color versions of one or more of the figures in this paper are available online at http://ieeexplore.ieee.org.

Digital Object Identifier 10.1109/TGRS.2008.916479

Observations of sea ice by the Electrically Scanning Microwave Radiometer (ESMR) onboard Nimbus-5 (1972–1976) and the Scanning Multispectral Microwave Radiometer (SMMR) onboard Nimbus-7 (1978–1987) were succeeded by the Special Sensor Microwave/Imager (SSM/I) onboard the Defense Meteorological Satellite Program (DMSP) satellites and the Advanced Microwave Scanning Radiometer-EOS (AMSR-E) onboard Aqua, producing daily sea ice concentration (SIC) products since 1987 and 2002, respectively [7]–[10].

SIC is defined as the ratio of an ice-covered area to the total area under consideration [11]. Archives of the Arctic and Antarctic SICs over more than two decades have been used to study the secular variations and fluctuations of sea ice area and extent [12], [13]. Although passive microwave sensors are typically of low spatial resolution (several tens of kilometers), they are efficient for sea ice monitoring because of the homogeneous and continuous observational capability over the entire polar region in daily basis [8], [14].

For the calculation of SSM/I SIC, two algorithms are widely used: one is the NASA Team (NT) algorithm [15], [16] and the other is the Bootstrap (BT) algorithm [17]. The NT2 algorithm [18] was initially developed for SSM/I as well and is being used as a standard algorithm for AMSR-E SIC. Many studies have focused on calibration and evaluation of such algorithms. Comiso *et al.* [19] showed that the BT algorithm produces higher value of SSM/I SIC than the NT algorithm, whereas SICs from Landsat-5 Thematic Mapper (TM), NOAA Advanced Very High Resolution Radiometer (AVHRR), and synthetic aperture radar (SAR) images were generally higher than BT-derived SIC. Markus and Dokken [20] have also compared SIC for central and edges of the Arctic sea ice from SAR images with SSM/I SIC calculated from the NT and NT2 algorithms, and they showed that NT2 is more correct than NT in the Arctic summer. Heinrichs *et al.* [21] have evaluated the AMSR-E NT2 algorithm at the ice edge in the Bering Sea by using RADARSAT-1 SAR and Moderate Resolution Imaging Spectroradiometer (MODIS) images, concluding that AMSR-E SIC showed good agreement with SAR and MODIS, but underestimated thin-ice areas.

Many other studies have also reported the disagreement of SICs between passive microwave sensors and other sensors, particularly for thin-ice areas. Most of them, however, used low- (> 100-m) to midresolution (> 30-m) satellite images such as SAR [22]–[24], Landsat TM [9], [25], Terra/Aqua MODIS [26], and NOAA AVHRR [27], [28]. Higher resolution

TABLE I
KOMPSAT-1 EOC SEA ICE IMAGES OF THE ANTARCTIC
(18 km × 18 km FOR EACH SCENE)

Orbit	Date	Center Location	Total Scenes	Cloud-free Scenes
1	2005/09/25	66.3S/52.8E	60	14
2	2005/10/01	66.3S/52.1E	62	0
3	2005/10/02	77.5S/156.6W	62	0
4	2005/10/05	77.5S/157.4W	61	40
5	2005/10/07	68.4S/150.7E	61	0
6	2005/10/08	77.5S/158.1W	61	5
7	2005/10/21	66.3S/52.5E	62	0
8	2005/10/24	66.3S/51.8E	61	0
9	2005/10/27	68.4S/150.3E	62	0
10	2005/10/30	68.4S/149.9E	61	0
11	2005/11/04	66.3S/53.1E	63	9
Total			676	68

sensors would be more favorable to observe various ice types, snow cover, cracks, and leads mixed in a relatively small region. Although there exist several satellite sensors of up to submeter resolution available commercially or scientifically, few studies have used them for polar research due to their high-cost low success rate of obtaining cloud-free images and low sun elevation.

In this paper, we report the evaluation of the SSM/I SIC derived from the NT algorithm and of the AMSR-E SIC from the NT2 algorithm by using 6-m-resolution optical images of the Antarctic sea ice obtained by the electronic optical camera (EOC) onboard the Korea Multi-Purpose Satellite-1 (KOMPSAT-1). We classified various sea ice types in EOC images, calculated SIC of each ice type, and compared the results with the SICs derived by the SSM/I NT algorithm and the AMSR-E NT2 algorithm which is provided by the National Snow and Ice Data Center (NSIDC).

II. METHODS

A. KOMPSAT-1 EOC Sea Ice Concentration

Launched in 1999, KOMPSAT-1 is Korea's first Earth-observing satellite and carries the EOC as its main payload. The EOC is a 6-m-resolution panchromatic (0.51–0.73-μm) pushbroom sensor with 18-km image swath and data storage of up to 2-min imaging (800 km) in ascending polar orbit. No direct broadcasting of data in the polar region is available due to the lack of local receiving facility. The images of the polar region were later downlinked to the satellite receiving station in Daejeon, Korea.

During September to November 2005, we obtained 676 scenes from 11 orbits along the Antarctic continental edges (Table I). Among them, only 68 cloud-free scenes from four orbits could be used for further analysis (Fig. 1). As the weather condition was not taken into consideration during the orbit selection process, the success rate of obtaining cloud-free optical image in this season was just over 10%.

The EOC images were first geocoded by using the ephemeris data of KOMPSAT-1. Geolocation errors of about 5–6 km were found and corrected by using Terra/Aqua MODIS images that were obtained at times and locations close to the EOC images, thus keeping the error within 1 km. This was accurate enough for the comparison of EOC images with passive microwave data, which were tens of kilometers in resolution.

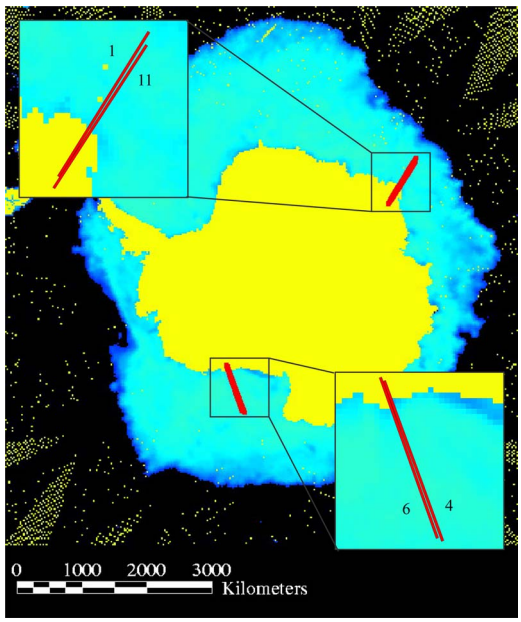

Fig. 1. KOMPSAT-1 EOC orbit numbers and image swaths that produced cloud-free sea ice images overlying the SSM/I SIC image of the Antarctic on September 25, 2005.

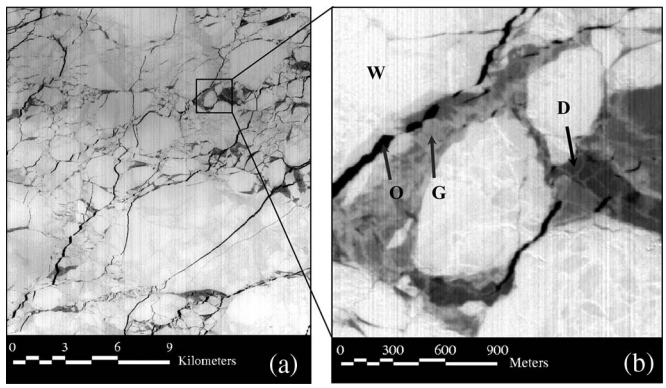

Fig. 2. Example of KOMPSAT-1 EOC image of the Antarctic sea ice. (a) A scene of EOC taken on October 5, 2005 (18 km × 18 km). (b) A classification example of EOC ice types into W, G, D, and O (2 km × 2 km).

Fig. 2(a) and (b) shows an example of sea ice imagery taken by the EOC on October 5, 2005. The image was taken during the Antarctic spring when sea ice began to melt slowly after its peak expansion. Sea ice blocks that were thickened during winter were mostly covered with snow (white). Leads were filled by refrozen thin ice with little snow cover (gray to dark gray), whereas narrow cracks exposed open water (black).

Sea ice types are classified into multiyear ice, first-year ice, young ice, and new ice, according to ice thickness and age [11]. Multiyear ice is sea ice that survived a summer melt and is thicker than 2–3 m. First-year ice is sea ice that is thicker than 30 cm. The visual appearance of multiyear and first-year ice is bright white due to its thickness, brine pockets, and snow cover. Young ice looks gray to gray white and is thicker than 10 cm.

New ice includes dark nilas, frazil ice, or grease ice that appears dark to dark gray and is thinner than 10 cm. As we have no *in situ* data of ice thickness or age, we could not use the World Meteorological Organization ice types directly to the EOC images. We divided ice into white ice (W), gray ice (G), dark-gray ice (D), and open water (O), according to gray-level and surface structural characteristics of sea ice in the EOC images.

Most of the Antarctic multiyear ice appears only in the Weddell Sea that was not imaged by the EOC in this paper. Therefore, W in the EOC images is mostly the first-year ice type (ice type A in the Antarctic [29]). Sea ice with heavy snow cover (ice type B) or surface snow/ice layering (ice type C) would look bright white and can be classified into W as well. When sea ice looks gray or dark gray, we can positively exclude it as being ice type A or B. This is because the ice must have formed relatively recently, for example, within a few days, with little time for snow accumulation resulting in low optical reflectivity [30]. Therefore, G and D, specifically of refrozen ice in leads and cracks, could be positively identified as young ice and new ice, respectively. The young ice and new ice types cause the well-known underestimation problem of the passive microwave sensors. In the springtime of the Antarctic, these thin-ice types appear mostly in ice leads or vicinity of ice cracks, which are observable by high-resolution sensors such as KOMPSAT-1 EOC. Therefore, G and D ice types in the EOC images are of particular interest in this paper to analyze the effect of thin ice to passive microwave sensors in the ice-thawing season of the Antarctic.

For the EOC image processing, cloud patches were initially masked out by visual inspection. We then applied the minimum-distance method for the supervised classification of sea ice types (Fig. 2). The overall accuracies of the classification [31] of the 68 EOC images showed the mean value of 96.2% with the standard deviation of 4.1% (Table II). The EOC SICs of each ice type were calculated by dividing the area of each ice type by the total area of a scene so that it could be compared with the results from the passive microwave sensors such as SSM/I and AMSR-E.

B. SSM/I Sea Ice Concentration From the NT Algorithm

The SSM/I is a passive microwave sensor composed of 19.35-, 37.0-, and 85.5-GHz dually polarized channels and a 22.235-GHz vertically polarized channel. It measures the incident radiation at the sensor, which is emitted and scattered by surfaces and volumes of sea ice. The NT algorithm was initially developed for NIMBUS-7 SMMR [16] and later adopted to the SSM/I [15], [32]. Using the 19.35-GHz dually polarized channels and the 37.0-GHz vertically polarized channel, the NT algorithm calculates the polarization ratio (PR) and the spectral gradient ratio (GR) as normalized differences of the observed brightness temperatures (TB) as follows:

$$\mathrm{PR}(19\mathrm{V}19\mathrm{H}) = [\mathrm{TB}(19\mathrm{V}) - \mathrm{TB}(19\mathrm{H})] \Big/ [\mathrm{TB}(19\mathrm{V}) + \mathrm{TB}(19\mathrm{H})] \quad (1)$$

$$\mathrm{GR}(37\mathrm{V}19\mathrm{V}) = [\mathrm{TB}(37\mathrm{V}) - \mathrm{TB}(19\mathrm{V})] \Big/ [\mathrm{TB}(37\mathrm{V}) + \mathrm{TB}(19\mathrm{V})]\,. \quad (2)$$

In the Arctic, the two ratios are used to produce ice concentrations of the multiyear and first-year ice types separately to be added into the total SIC. As the characteristic of microwave radiation of Antarctic sea ice differs from that of Arctic sea ice [33], [34], the NT algorithm calculates ice concentration of ice types A and B in the Antarctic. It is known that the NT algorithm generates error in the ice edges [35], [36], snow layer [18], and wet and thin-ice surface [37], [38]. The daily SSM/I SIC product of the Antarctic used in this paper is from the NT algorithm with 25-km grid spacing and is the sum of ice types A and B [19]. SSM/I SIC data are the daily-averaged value of SICs obtained from multiple orbits of the DMSP F13 satellite.

C. AMSR-E SIC From the NT2 Algorithm

AMSR-E has six dually polarized frequencies (6.9, 10.7, 18.7, 23.8, 36.5, and 89 GHz). It also provides the daily SIC of the Antarctic, with 12.5-km resolution calculated from the NT2 algorithm by summation of ice types A, B, and C [18]. Using 18.7-GHz dually polarized channels, 36.5-GHz vertically polarized channel, and 89.0-GHz dually polarized channels, the NT2 algorithm calculates the ratios that are similar to (1) and (2) and, additionally, the rotated polarization and the difference between the gradient ratios [18]. It has been reported that the NT2 algorithm can solve the problem of the NT algorithm that underestimates the SIC of snow-covered or wet ice. The NT2 algorithm additionally detects ice type C that has inhomogeneous surface layer with significant complex scattering within the snow cover, which is frequently underestimated by the NT algorithm. Further improvement has been implemented to take into account for thin ice and to overcome the underestimation problem of passive microwave sensors in the presence of new ice [29].

D. Spatiotemporal Standard Deviation of Passive Microwave Sea Ice Concentrations (σ_{ST})

In the process of comparison, we extract SSM/I and AMSR-E SICs of the same observation date and location as the KOMPSAT-1 EOC images. Problems may arise due to the narrow swath of EOC images and diurnal variability of sea ice during the time difference of data acquisition between EOC and passive microwave sensors.

As the size of an EOC image (18 km $\times$ 18 km) is similar to the pixel size of SSM/I (25 km) and AMSR-E (12.5 km), no statistical measure could be obtained to test the reliability of data with just a single-point comparison for each scene of EOC. Contrary to low-resolution sensors with wide swath such as AVHRR or SAR images, the narrow-swath problem is inherent to high-resolution images such as EOC images.

The daily products of SSM/I and AMSR-E SICs are calculated by temporal averaging of values from several orbits. Therefore, direct comparison of the passive microwave data with the EOC data obtained in a single orbit could yield significant errors caused by rapid movement of sea ice, changes of sea ice surface state, and weather effects. AMSR-E SIC provides the daytime, nighttime, and daily-averaged products separately. By using only the daytime (ascending pass) data

TABLE II
CLASSIFICATION ACCURACIES OF THE 68 KOMPSAT-1 EOC SEA ICE IMAGES

Accuracy / EOC sea ice	User's Accuracy		Producer's Accuracy		Overall Accuracy	
	Mean	STD	Mean	STD	Mean	STD
White ice (W)	97.9%	4.1%	98.1%	4.2%	96.2%	4.1%
Grey ice (G)	92.6%	9.1%	92.1%	10.9%		
Dark-grey ice (D)	92.4%	9.5%	93.7%	8.7%		
Open water (O)	97.7%	4.1%	97.2%	3.9%		

for the comparison with EOC images, we can expect better correlation due to the shorter temporal difference of less than 4 h between two sensors. In the case of SSM/I SIC, however, only the daily-averaged product is available for us, and we have no alternative that is similar to AMSR-E. The difference of the daytime and daily-averaged AMSR-E SIC products will be analyzed in the following section.

To overcome such restrictions on the data, we calculated spatiotemporal mean ($\overline{S}_{\mathrm{ST}}$) and standard deviation (σ_{ST}) of passive microwave SICs using a $3 \times 3 \times 3$ cubic-pixel averaging window as follows:

$$\overline{S}_{\mathrm{ST}} = \frac{1}{27} \sum_{i=1}^{3} \sum_{j=1}^{3} \sum_{k=1}^{3} \mathrm{SIC}_{ijk} \tag{3}$$

$$\sigma_{\mathrm{ST}}^2 = \frac{1}{27} \sum_{i=1}^{3} \sum_{j=1}^{3} \sum_{k=1}^{3} (\mathrm{SIC}_{ijk} - \overline{S}_{\mathrm{ST}})^2 \tag{4}$$

where SIC_{ijk} indicates SIC. The subscript i is related to a temporal averaging window of three-pixel size composed of the day before the EOC acquisition, the day, and the day after, whereas j and k form a 3×3 spatial averaging window with pixels neighboring the location of the EOC image. σ_{ST} is inversely proportional to temporal stability and spatial homogeneity of the passive microwave SIC data. This value will provide a valuable criterion on the fidelity of comparative data interpretation in such a way that only the passive microwave SICs with low σ_{ST} should be used for the comparison with the EOC SIC to avoid uncertainties that may arise from diurnal variation of sea ice and spatial mismatch of multisatellite data.

III. RESULTS AND DISCUSSIONS

We compared various combinations of the EOC SIC such as W, W + G, and W + G + D with passive microwave SICs. The vertical error bar of each data point in Figs. 3 and 4 is centered at $\overline{S}_{\mathrm{ST}}$ and has the length of $2\sigma_{\mathrm{ST}}$. Black data points in Figs. 3–6, and 8 are stable SICs having σ_{ST}'s that are less than 2.5%, which could be considered temporally stable and spatially homogeneous so that we can compare SICs from EOC and passive microwave sensors directly. White data points are unstable SICs with σ_{ST}'s that are more than 2.5%. The sea ice state on these points can be regarded as temporally unstable or spatially inhomogeneous, and the direct comparison of EOC and the passive microwave SICs could be biased, rendering it less significant for data interpretation. The mean and standard deviation of the difference (error) between passive microwave sensors and EOC ($\overline{E}$ and σ_E) were calculated for each comparison with different combinations of EOC ice types. The statistical values were calculated twice: one for all points and the other for black points, which are shown in each figure and summarized in Table III.

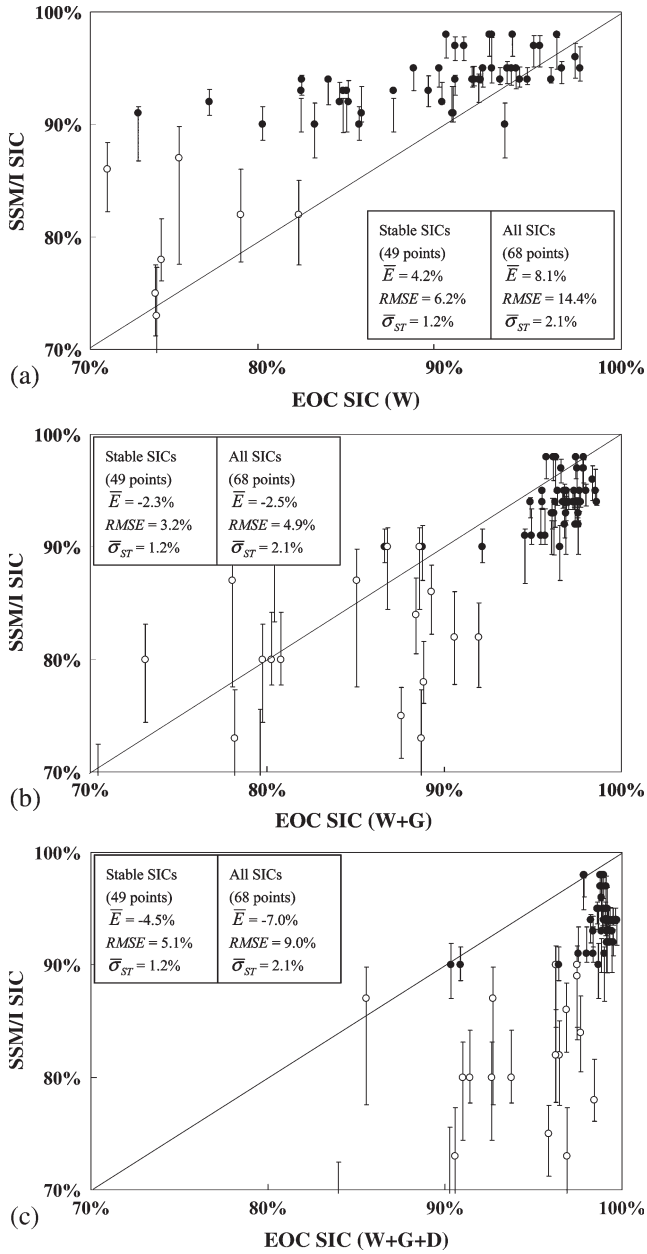

Fig. 3. Comparison of SSM/I SIC with EOC SICs of (a) W, (b) W + G, and (c) W + G + D. Stable (black) points are SIC with $\sigma_{\mathrm{ST}} < 2.5\%$. SSM/I SIC correlates well with EOC SIC of W + G in (b) both for stable SICs and all SICs.

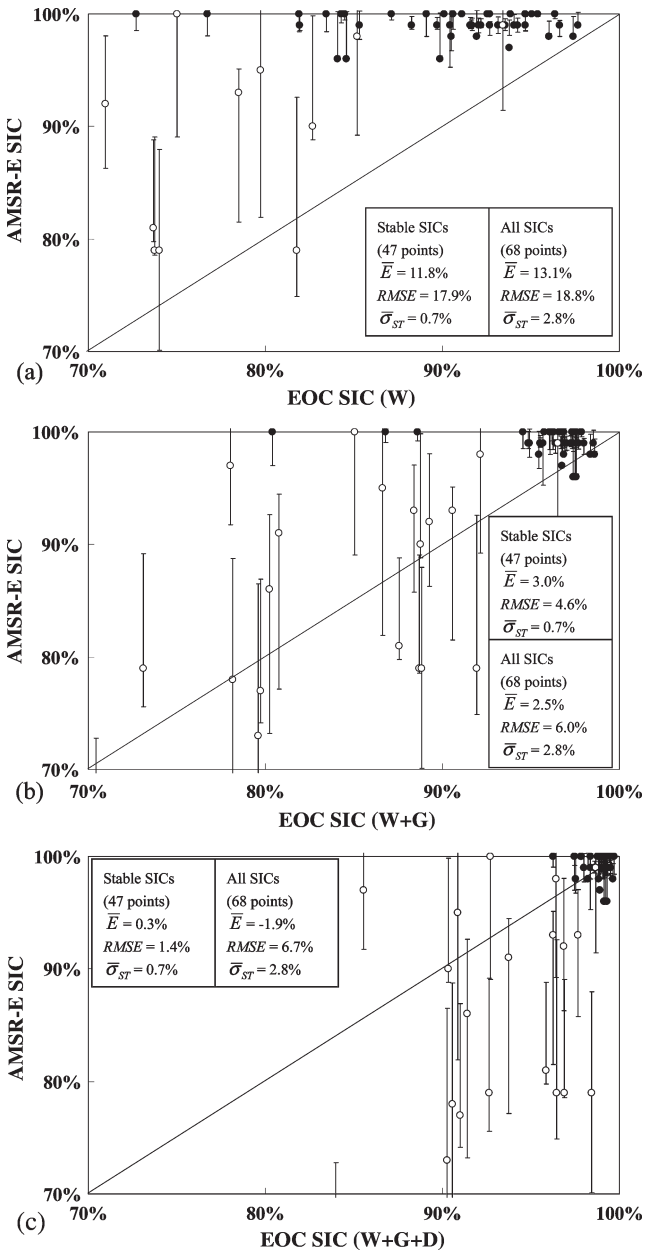

Fig. 4. Comparison of AMSR-E SIC with EOC SICs of (a) W, (b) W + G, and (c) W + G + D. AMSR-E SIC of stable (black) points correlates well with the summation of all ice types (W + G + D) of EOC SIC in (c), indicating that AMSR-E SIC responds to D in addition to W and G.

A. Comparison of EOC and SSM/I Sea Ice Concentrations

Fig. 3 shows the comparison of SSM/I SIC with various EOC ice types. The data points and statistical values in Fig. 3(a) indicate that SSM/I SICs have higher values than EOC SICs of W only. It is obvious that SSM/I SICs respond to other EOC ice types as well than just W. On the other hand, the comparison of SSM/I SIC with EOC SIC of all types (W + G + D), as shown in Fig. 3(c), degraded all statistical values, indicating that all EOC ice types do not respond equally to SSM/I SIC. When we compared SSM/I SIC with EOC SIC of W + G, excluding D as shown in Fig. 3(b), all statistics indicated the best match. The $\overline{E}$ and rmse have the lowest values of -2.3% and 3.2% for stable SICs and -2.5% and 4.9% for all SICs, respectively, as shown

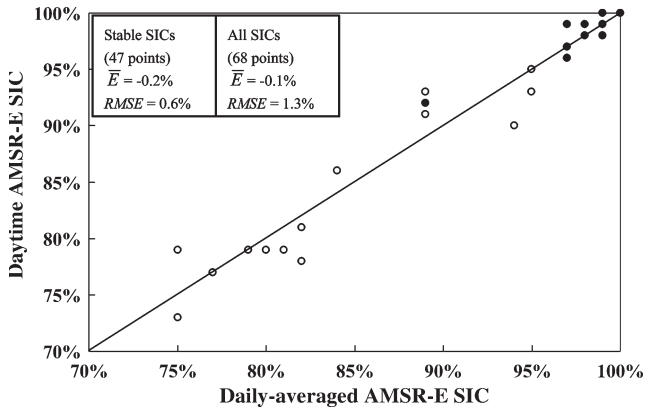

Fig. 5. Comparison of the daytime and the daily-averaged AMSR-E SICs. The difference is negligible in terms of accuracy required in this paper.

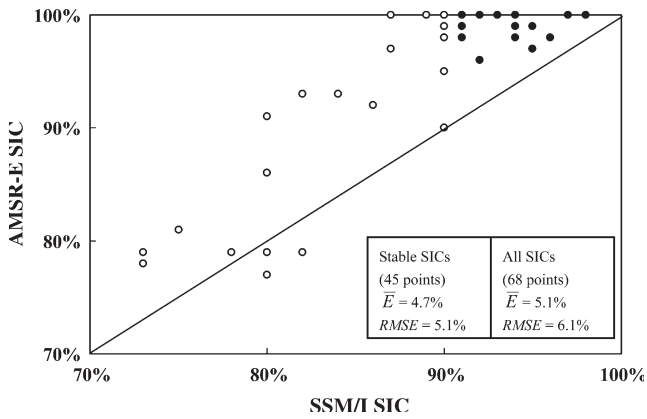

Fig. 6. Comparison of SSM/I and AMSR-E SIC data points used for the comparisons with EOC SIC. AMSR-E SIC shows generally higher value than SSM/I SIC by 4.7% due to the detection of ice type C and thin ice for the Antarctic sea ice in the AMSR-E NT2 algorithm, in addition to ice types A and B in the SSM/I NT algorithm.

in Fig. 3(b) and Table III. Therefore, we conclude that SSM/I SIC responds primarily to W + G and less to D.

Slightly different from the well-known underestimation problem of SSM/I SICs in areas of young and new ice, our analysis showed that the SSM/I NT algorithm may respond to the G (young) ice type as well. The rationale of this conclusion is that the ice area of W in the EOC images cannot explain the higher value of SSM/I SIC. The G type (or young ice) that is frequently observed in the leads and near the cracks, particularly in the Antarctic spring, should be counted as well for better correlation with SSM/I SIC.

B. Comparison of EOC and AMSR-E Sea Ice Concentrations

Similar comparisons were performed between AMSR-E and EOC SICs in Fig. 4. All types of EOC SIC (W + G + D) were better matched with AMSR-E SIC than other combinations of EOC ice types, as shown in Fig. 4(c) and Table III, having the lowest $\overline{E}$ and rmse of 0.3% and 1.4%, respectively, for stable data points. For all points, $\overline{E}$ showed the best match in the case of EOC (W + G + D) with the value of -1.9%, whereas rmse was best (6.0%) for the case of EOC (W + G). As the statistics obtained with the stable SICs were recognized as more reliable

TABLE III
STATISTICS ON THE COMPARISONS BETWEEN SSM/I NT, AMSR-E NT2, AND EOC SICs. $\overline{E}$ AND RMSE ARE THE MEAN AND ROOT-MEAN-SQUARE ERROR, RESPECTIVELY. $\overline{\sigma}_{\mathrm{ST}}$ IS THE MEAN OF SPATIOTEMPORAL STANDARD DEVIATION OF PASSIVE MICROWAVE SIC. THE BEST MATCHES ARE HIGHLIGHTED IN BOLD CHARACTERS

PM Sensors / EOC	Algorithm	SSM/I NT			AMSR-E NT2		
	Stability	Stable	Unstable	All	Stable	Unstable	All
	$\overline{\sigma}_{ST}$	1.2%	4.2%	2.1%	0.7%	7.5%	2.8%
W	$\overline{E}$	4.2%	18.1%	8.1%	11.8%	16.2%	13.1%
	RMSE	6.2%	25.5%	14.4%	17.9%	21.2%	18.8%
W+G	$\overline{E}$	**-2.3%**	-3.1%	-2.5%	3.0%	1.3%	2.5%
	RMSE	**3.2%**	7.9%	4.9%	4.6%	8.7%	6.0%
W+G+D	$\overline{E}$	-4.5%	-13.3%	-7.0%	**0.3%**	-7.3%	-1.9%
	RMSE	5.1%	14.8%	9.0%	**1.4%**	12.2%	6.7%

than those with the all-point case, we concluded that AMSR-E SIC responds not only to W and G but also to D.

C. Daily-Averaged Versus Daytime AMSR-E Sea Ice Concentrations

The time difference of observations between EOC and passive microwave sensors could reduce the correlation due to diurnal variation of sea ice. Therefore, we reanalyzed the data using the daytime AMSR-E data in addition to the daily-averaged data shown in the previous section. We expected a better correlation between EOC and AMSR-E obtained with time difference of less than 4 h. If this were the case, the aforementioned comparisons of EOC with the daily-averaged AMSR-E and SSM/I data would be unreliable. However, the correlation was not improved significantly enough to alter the conclusions we have made. In fact, there exist a lot of differences between the daytime and daily-averaged AMSR-E SICs at the margins of the Antarctic sea ice. At the locations of EOC data, however, the difference was negligibly small with $\overline{E}$ and rmse of -0.2% and 0.6% for stable points and -0.1% and 1.3% for all data points (Fig. 5), respectively. This is because we have already chosen the "stable" data points by applying a 2.5% criterion to the σ_{ST} of passive microwave data. As mentioned earlier, σ_{ST}'s at the location and time of the EOC data take were spatially homogeneous over 3×3 neighboring pixels and also temporally stable for three days (the day before, the day, and the day after the EOC data take). The use of σ_{ST} criterion to SSM/I as well as AMSR-E is an effective method to overcome the problem of temporal discrepancy that is inherent to a comparative study in which the data from multiple satellites should be involved.

D. Comparison of SSM/I and AMSR-E Sea Ice Concentrations

Through the comparison of SICs between EOC and passive microwave sensors, it was found that both SSM/I and AMSR-E respond to G as well as W. The two algorithms seem to respond to the G type as well that is similar to young ice. Moreover, AMSR-E SIC includes D as well, whereas SSM/I SIC does not.

The comparison of SSM/I and AMSR-E SICs in Fig. 6 indicates that most AMSR-E SIC values were higher than SSM/I SIC values by 4.7% for stable SICs. The difference came from the fact that the SSM/I NT algorithm discriminates ice types A and B, whereas the AMSR-E NT2 algorithm detects ice type C and also thin ice [18], [29].

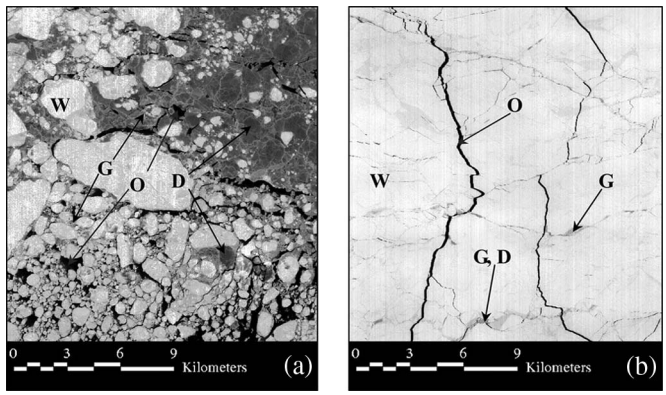

Fig. 7. Examples of EOC scenes (18 km × 18 km) with different ice concentrations. (a) EOC image with large portion of D (W: 51.8%, G: 29.0%, D: 13.0%, and O: 6.2%) taken on September 25, 2005 (AMSR-E: 89% and SSM/I: 80%). (b) EOC image with little D (W: 97.4%, G: 1.0%, D: 0.5%, and O: 1.1%) taken on October 5, 2005 (AMSR-E: 98% and SSM/I: 96%).

It is interesting to notice from Figs. 3 and 4 and Table III that, for unstable SICs, the mean of σ_{ST}, i.e., $\overline{\sigma}_{\mathrm{ST}}$ of AMSR-E, was higher than that of SSM/I (7.5% versus 4.2%). This also indicates that the AMSR-E NT2 algorithm is more sensitive to new ice type. D is thought to be a thin ice of which the surface temperature is near the freezing temperature of O ice type [39]. The growth rate of thin ice increases with wind speed [40], and the spatiotemporal variability is higher than those of W or G type. Thin D experiences daily thawing and refreezing processes in the springtime [41] with a relatively high mobility driven by current or wind, resulting in higher $\overline{\sigma}_{\mathrm{ST}}$ of AMSR-E SIC than that of SSM/I SIC.

E. Contributions of Ice Type C and Thin Ice to the Difference of AMSR-E and SSM/I Sea Ice Concentrations

Fig. 7 shows examples of EOC images with different portions of D SIC. The D ice type in the EOC image is recently frozen thin-ice layers composed of grease ice, dark nilas, or frazil ice with little snow cover. Fig. 7(a) is an EOC image obtained on September 25, 2005, which comprises 51.8% of W, 29.0% of G, and 13.0% of D. The SSM/I and AMSR-E SICs of this image were 80% and 89%, respectively, having 9% difference. Fig. 7(b) is another example of EOC image with little D type, which was acquired on October 5, 2005. The scene includes 97.4% of W, 1.0% of G, and 0.5% of D. SSM/I and AMSR-E SICs were 96% and 98%, respectively, showing

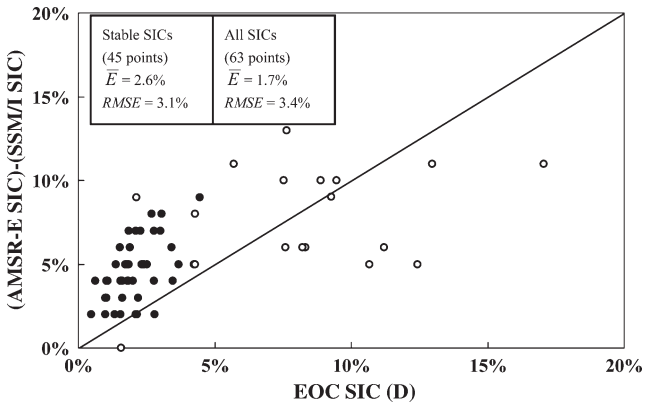

Fig. 8. Comparison of the difference of AMSR-E SIC and SSM/I SIC with EOC SIC of D.

2% difference between AMSR-E and SSM/I SICs. These two examples show that the difference of SICs between AMSR-E and SSM/I increases as the ice area of D increases.

This relationship can be also found in Fig. 8 showing the comparison of EOC SIC (D) and the difference of AMSR-E and SSM/I. The mean difference of 4.7% for stable SICs between AMSR-E and SSM/I found in Fig. 6 presumably originates from the improved detection capability of the AMSR-E NT2 algorithm for ice type C and thin (new) ice. Ice type C would look white, similar to ice types A and B, so that it would be merged into the category of EOC W or G, whereas thin (new) ice can be connected to EOC D. From the $\overline{E}$ values in Figs. 6 and 8, we conclude that approximately 2.6% out of the 4.7% difference can be attributed to the superiority of the AMSR-E NT2 algorithm compared with the SSM/I NT algorithm in the detection of ice type C, whereas the remaining (2.1%) difference might have come from the enhancement of thin-ice detection in the NT2 algorithm in this particular data set.

IV. Conclusion

To evaluate SIC from passive microwave sensors, we obtained 68 cloud-free scenes of KOMPSAT-1 EOC (panchromatic 6-m resolution and 18-km swath) in the Antarctic spring in 2005. We classified sea ice in the EOC images into W, G, and D sea ice types, calculated SIC of each ice type, and compared them with SICs calculated by the SSM/I NT and AMSR-E NT2 algorithms. We also calculated the spatiotemporal standard deviation (σ_{ST}) of passive microwave SICs using $3 \times 3 \times 3$ cubic window and used it as a criterion for uncertainties that may rise from the time difference of multiple satellite passes and diurnal variability of sea ice.

Comparison of the AMSR-E SICs obtained by daytime passes and daily-averaged values at the locations of EOC images showed very little difference with the rmse values of 0.6% for stable points ($\sigma_{\mathrm{ST}} < 2.5\%$). Therefore, the use of daily-averaged SICs of SSM/I and AMSR-E, instead of single-orbit passive microwave data, is proven to be valid for the comparison with single-orbit EOC image. The usefulness of σ_{ST} as a criterion for the selection of stable SICs has also been proven.

Comparisons of EOC with passive microwave sensors showed that SSM/I SIC calculated by the NT algorithm was best correlated to EOC W + G (mean difference of −2.3% and rmse of 3.2), whereas AMSR-E SIC calculated by the AMSR-E NT2 algorithm was best correlated to W + G + D (mean difference of 0.3% and rmse of 1.4%). It is suggested that SSM/I SIC responds not only to ice types A and B (W) but also to young ice (G), whereas AMSR-E SIC includes all the EOC ice types including thin (new) ice (D). Approximately 4.7% difference of SICs between AMSR-E and SSM/I was statistically attributed to thin (dark-gray) ice by 2.6% and to ice type C by 2.1%. This result is in accordance with the improvement of the AMSR-E NT2 algorithm for the detection of thin-ice area and ice type C [29].

Despite the absence of ground reference data such as ice thickness or surface condition at the time of satellite data acquisition, we could evaluate the different characteristics of SSM/I and AMSR-E SICs by using high-resolution optical EOC images in the Antarctic spring. The use of high-resolution images for the evaluation of passive microwave SICs should be extended to other seasons and regions to provide a comprehensive comparison. This could be possible through a continuous archiving of high-resolution optical images in addition to active microwave sensors such as SAR or altimeter and *in situ* data collection.

Acknowledgment

The authors would like to thank the two reviewers for their very helpful comments that substantially improved the interpretation and analysis of the data. The KOMPSAT-1 EOC data set was provided by the Korea Aerospace Research Institute. The SSM/I and AMSR-E SIC data were obtained from the Earth Observing System data gateway at NSIDC.

References

[1] R. G. Barry, M. C. Serreze, J. A. Maslanik, and R. H. Preller, "The arctic sea ice–climate system: Observations and modeling," *Rev. Geophys.*, vol. 31, no. 4, pp. 397–422, Nov. 1993.

[2] R. G. Barry, "The role of snow and ice in the global climate system: A review," *Polar Geogr.*, vol. 26, no. 3, pp. 235–246, Jul. 2002.

[3] P. Lemke, M. Harder, and M. Hilmer, "The response of Arctic sea ice to global change," *Clim. Change*, vol. 46, no. 3, pp. 277–287, Aug. 2000.

[4] J. S. Singarayer, J. L. Bamber, and P. J. Valdes, "Twenty-first-century climate impacts from a declining Arctic sea ice cover," *J. Clim.*, vol. 19, no. 7, pp. 1109–1115, Apr. 2006.

[5] K. Y. Vinnikov, A. Robock, R. J. Stouffer, J. E. Walsh, C. L. Parkinson, D. J. Cavalieri, J. F. B. Mitchell, D. Garrett, and V. F. Zakharov, "Global warming and Northern Hemisphere sea ice extent," *Science*, vol. 286, no. 5446, pp. 1934–1937, Dec. 1999.

[6] H. J. Zwally, C. L. Parkinson, and J. C. Comiso, "Variability of Antarctic sea ice and changes in carbon dioxide," *Science*, vol. 220, no. 4601, pp. 1005–1012, 1983.

[7] D. J. Cavalieri, C. L. Parkinson, P. Gloersen, J. C. Comiso, and H. J. Zwally, "Deriving long-term time series of sea ice cover from satellite passive-microwave multisensor data sets," *J. Geophys. Res.*, vol. 104, no. C7, pp. 15 803–15 814, Jul. 1999.

[8] D. J. Cavalieri, P. Gloersen, C. L. Parkinson, J. C. Comiso, and H. J. Zwally, "Observed hemispheric asymmetry in global sea ice changes," *Science*, vol. 278, no. 5340, pp. 1104–1106, Nov. 1997.

[9] D. J. Cavalieri, T. Markus, D. K. Hall, A. J. Gasiewski, M. Klein, and A. Ivanoff, "Assessment of EOS Aqua AMSR-E arctic sea ice concentrations using Landsat-7 and airborne microwave imagery," *IEEE Trans. Geosci. Remote Sens.*, vol. 44, no. 11, pp. 3057–3069, Nov. 2006.

[10] D. J. Cavalieri, T. Markus, J. A. Maslanik, M. Sturm, and E. Lobl, "March 2003 EOS Aqua AMSR-E Arctic sea ice field campaign," *IEEE Trans. Geosci. Remote Sens.*, vol. 44, no. 11, pp. 3003–3008, Nov. 2006.

[11] *WMO Sea Ice Nomenclature*, 1970 ed. Geneva, Switzerland: Secr. World Meteorol. Org., 1970.
[12] E. Bjørgo, O. M. Johannessen, and M. W. Miles, "Analysis of merged SMMR–SSMI time series of Arctic and Antarctic sea ice parameters 1978–1995," *Geophys. Res. Lett.*, vol. 24, no. 4, pp. 413–416, 1997.
[13] H. J. Zwally, J. C. Comiso, C. L. Parkinson, D. J. Cavalieri, and P. Gloersen, "Variability of Antarctic sea ice 1979–1998," *J. Geophys. Res.*, vol. 107, no. C5, May 2002. DOI: 10.1029/2000JC000733.
[14] P. Gloersen and W. J. Campbell, "Variations in the Arctic, Antarctic, and global sea ice covers during 1978–1987 as observed with the Nimbus-7 scanning multichannel microwave radiometer," *J. Geophys. Res.*, vol. 93, no. C9, pp. 10 666–10 674, 1988.
[15] D. J. Cavalieri, J. P. Crawford, M. R. Drinkwater, D. T. Eppler, L. D. Farmer, R. R. Jents, and C. C. Wackerman, "Aircraft active and passive microwave validations of sea ice concentrations from the DMSP SSM/I," *J. Geophys. Res.*, vol. 96, no. C12, pp. 21 989–22 008, 1991.
[16] D. J. Cavalieri, P. Gloersen, and W. J. Campbell, "Determination of sea ice parameters with the NIMBUS-7 SMMR," *J. Geophys. Res.*, vol. 89, no. D4, pp. 5355–5369, 1984.
[17] J. C. Comiso, "Characteristics of arctic winter sea ice from satellite multispectral microwave observation," *J. Geophys. Res.*, vol. 91, no. C1, pp. 975–994, 1986.
[18] T. Markus and D. J. Cavalieri, "An enhancement of the NASA team sea ice algorithm," *IEEE Trans. Geosci. Remote Sens.*, vol. 38, no. 3, pp. 1387–1398, May 2000.
[19] J. C. Comiso, D. J. Cavalieri, C. L. Parkinson, and P. Gloersen, "Passive microwave algorithms for sea ice concentration: A comparison of two techniques," *Remote Sens. Environ.*, vol. 60, no. 3, pp. 357–384, Jun. 1997.
[20] T. Markus and S. T. Dokken, "Evaluation of late summer passive microwave Arctic sea ice retrievals," *IEEE Trans. Geosci. Remote Sens.*, vol. 40, no. 2, pp. 348–356, Feb. 2002.
[21] J. F. Heinrichs, D. J. Cavalieri, and T. Markus, "Assessment of the AMSR-E sea ice concentration product at the ice edge using RADARSAT-1 and MODIS imagery," *IEEE Trans. Geosci. Remote Sens.*, vol. 44, no. 11, pp. 3070–3080, Nov. 2006.
[22] G. I. Belchansky and D. C. Douglas, "Seasonal comparisons of sea ice concentration estimates derived from SSM/I, OKEAN, and RADARSAT data," *Remote Sens. Environ.*, vol. 81, no. 1, pp. 67–81, Jul. 2002.
[23] S. Kern, L. Kaleschke, and D. A. Clausi, "A comparison of two 85-GHz SSM/I ice concentration algorithms with AVHRR and ERS-2 SAR imagery," *IEEE Trans. Geosci. Remote Sens.*, vol. 41, no. 10, pp. 2294–2306, Oct. 2003.
[24] M. Shokr and T. Markus, "Comparison of NASA Team2 and AES-York ice concentration algorithms against operational ice charts from the Canadian ice service," *IEEE Trans. Geosci. Remote Sens.*, vol. 44, no. 8, pp. 2164–2175, Aug. 2006.
[25] A. P. Worby and J. C. Comiso, "Studies of the Antarctic sea ice edge and ice extent from satellite and ship observations," *Remote Sens. Environ.*, vol. 92, no. 1, pp. 98–111, Jul. 2004.
[26] C. Drüe and G. Heinemann, "Accuracy assessment of sea ice concentrations from MODIS using in-situ measurements," *Remote Sens. Environ.*, vol. 95, no. 2, pp. 139–149, Mar. 2005.
[27] W. J. Emery, C. Fowler, and J. Maslanik, "Arctic sea ice concentrations from Special Sensor Microwave Imager and Advanced Very High Resolution Radiometer satellite data," *J. Geophys. Res.*, vol. 99, no. C9, pp. 18 329–18 342, Sep. 1994.
[28] W. J. Emery, M. Radebaugh, C. Fowler, D. J. Cavalieri, and K. Steffen, "A comparison of sea ice parameters computed from Advanced Very High Resolution Radiometer, Landsat imagery and from passive microwave radiometer," *J. Geophys. Res.*, vol. 96, no. C12, pp. 22 075–22 085, 1991.
[29] J. C. Comiso, D. J. Cavalieri, and T. Markus, "Sea ice concentration, ice temperature, and snow depth using AMSR-E data," *IEEE Trans. Geosci. Remote Sens.*, vol. 41, no. 2, pp. 243–252, Feb. 2003.
[30] R. A. Massom, H. Eicken, C. Hass, M. O. Jeffries, M. R. Drinkwater, M. Sturm, A. P. Worby, X. Wu, V. I. Lytle, and S. Ushio, "Snow on Antarctic sea ice," *Rev. Geophys.*, vol. 39, no. 3, pp. 413–445, Aug. 2001.
[31] J. R. Jensen, *Introductory Digital Image Processing : A Remote Sensing Perspective*, 3rd ed. Englewood Cliffs, NJ: Prentice-Hall, 2005.
[32] P. Gloersen and D. J. Cavalieri, "Reduction of weather effects in the calculation of sea ice concentration from microwave radiances," *J. Geophys. Res.*, vol. 91, no. C3, pp. 3913–3919, 1986.
[33] S. F. Ackley, A. J. Gow, K. R. Buck, and K. M. Golden, "Sea ice studies in the Weddell Sea aboard USCGC polar sea," *Antarctic J. U. S.*, vol. 15, no. 5, pp. 84–86, 1980.
[34] P. Wadhams, M. A. Lange, and S. F. Ackley, "The ice thickness distribution across the Atlantic sector of the Antarctic Ocean in midwinter," *J. Geophys. Res.*, vol. 92, no. C13, pp. 14 535–14 552, 1987.
[35] K. C. Partington, "A data fusion algorithm for mapping sea ice concentration from Special Sensor Microwave/Imager data," *IEEE Trans. Geosci. Remote Sens.*, vol. 38, no. 4, pp. 1947–1958, Jul. 2000.
[36] J. Haarpaintner and G. Spreen, "Use of enhanced-resolution QuikSCAT/SeaWinds data for operational ice services and climate research: Sea ice edge, type, concentration, and drift," *IEEE Trans. Geosci. Remote Sens.*, vol. 45, no. 10, pp. 3131–3137, Oct. 2007.
[37] J. A. Maslanik, "Effects of weather on the retrieval of sea ice concentration and ice type from passive microwave data," *Int. J. Remote Sens.*, vol. 13, no. 1, pp. 37–54, Jan. 1992.
[38] W. N. Meier, "Comparison of passive ice concentration algorithm retrievals with AVHRR imagery in Arctic peripheral seas," *IEEE Trans. Geosci. Remote Sens.*, vol. 43, no. 6, pp. 1324–1337, Jun. 2005.
[39] R. Kwok, J. C. Comiso, S. Martin, and R. Drucker, "Ross Sea polynyas: Response of ice concentration retrievals to large areas of thin ice," *J. Geophys. Res.*, vol. 112, no. C12, 2007. DOI: 10.1029/2006JC003967.
[40] S. Andersen, L. Kaleschke, G. Heygster, and L. T. Pedersen, "Intercomparison of passive microwave sea ice concentration retrievals over the high-concentration Arctic sea ice," *J. Geophys. Res.*, vol. 112, no. C8, 2007. DOI: 10.1029/2006JC003543.
[41] J. K. Ehn, M. A. Granskog, T. Papakyriakou, R. Galley, and D. G. Barber, "Surface albedo observations of Hudson Bay (Canada) landfast sea ice during the spring melt," *Ann. Glaciol.*, vol. 44, no. 1, pp. 23–29, Nov. 2006.

Hoonyol Lee (S'99–A'01) was born in Kwangju, Korea, in 1969. He received the B.S. degree in geology and the M.S. degree in geophysics from Seoul National University, Seoul, Korea, in 1995 and 1997, respectively, and the Ph.D. degree in radar remote sensing from Imperial College London (University of London), London, U.K., in 2001.

From 2001 to 2003, he was a Postdoctoral Research Associate with Imperial College London. From 2003 to 2004, he was a Senior Researcher with the Korea Institute of Geoscience and Mineral Resources, Daejeon. Since 2004, he has been an Assistant Professor with the Department of Geophysics, Kangwon National University, Chuncheon, Korea. His research interests include a wide range of remote sensing such as SAR, interferometry, polarimetry, and optical remote sensing. He developed an educational SAR focusing processor, a SAR ocean processor, a polarimetric scatterometer system, and a ground-based SAR system.

Prof. Lee was awarded the Interactive Session Prize Paper Award at the 1999 IEEE International Geoscience and Remote Sensing Symposium, Hamburg, Germany, for his paper that was coauthored by Dr. J. G. Liu. He was supported by the Korean Ministry of Education Scholarship, the Overseas Research Student Award from the Committee of Vice-Chancellor and Principals, U.K., and the Chevening Scholarship from the British Embassy in Korea for his Ph.D. study.

Hyangsun Han (S'06) was born in Chuncheon, Korea, in August 1982. He received the B.A. and M.A. degrees in geophysics from Kangwon National University, Chuncheon, in 2006 and 2008, respectively.

His past and current research interests include remote sensing of polar sea ice, ocean and land surfaces, and various applications of remotely sensed data.

Mr. Han received Student Paper Awards at the Korea Remote Sensing Symposia in 2006 and 2007.